Mechanistic Influence of Nanometer Length-Scale Surface Chemistry on DNA Hybridization

Payel Das[*,†] **and Sufi Zafar**[*,‡]

[†]Computational Biology Center, IBM Thomas J. Watson Research Center, 1101 Kitchawan Road, Yorktown Heights, New York 10598, United States and [‡]IBM Thomas J. Watson Research Center, 1101 Kitchawan Road, Yorktown Heights, New York 10598, United States

ABSTRACT Hybridization of surface-immobilized oligonucleotides to their complementary counterparts is central to the rational design of novel nanodevices and DNA sensors. In this study, we have adopted a unified approach of combining sensing experiments with molecular dynamics simulations to characterize the hybridization of a 23 nucleotide long single-strand probe DNA tethered to a gold surface. Experiments indicate significant conformational changes of DNA in close vicinity (~1 nm) of the gold surface upon hybridization and also conformational heterogeneity within hybridized DNA, consistent with simulation results. Simulations show that the conformational heterogeneity on a gold surface arises due to stabilization of surface-adsorbed partial and full duplexes, resulting in impeded hybridization in comparison to what observed on a repulsive surface. Furthermore, these simulations indicate that hybridization could be improved by tuning the nonspecific adsorption on a nanopatterned surface with an optimal patterning length. Simulations were performed on the probe tethered to gold nanodots of varying (2−8 nm) diameter. An improved hybridization of the present probe sequence was only observed for the 6 nm gold dots patterned on a repulsive surface. Results reveal that the 2D nanoconfinement provided by the 6 nm gold dot is optimal for reducing conformational heterogeneity for the specific sequence used in this study. Thus, improved DNA hybridization can be achieved on a gold nanodot patterned repulsive surface, where the optimal dot diameter will depend on the probe length and sequence. In summary, this study provides mechanistic insights onto hybridization on gold and offers a unique method toward improved hybridization on a nanopatterned surface with an optimized patterning length.

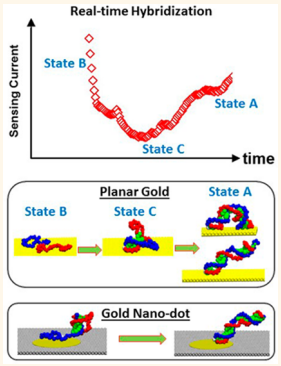

KEYWORDS: DNA · gold · surface-mediated self-assembly · real-time hybridization · molecular dynamics simulations

Surface hybridization, in which an immobilized probe single-stranded DNA (ss-DNA) of known sequence recognizes the complementary target ss-DNA (c-DNA) molecule, is central to DNA biosensing technologies and novel nanodevices. These techniques are being extensively applied in a number of important fields such as genotyping, gene expression profiling, and biological detection.[1−3] Hybridization at the solid−liquid interface can be significantly promoted by nonspecific adsorption of the target ss-DNA and the consequent two-dimensional search.[4] Several other factors such as probe density,[5−8] probe[9] and linker length,[10] surface topology,[11] and surface chemistry[12] further affect surface hybridization, thus making hybridization on surface more complicated than that in solution. However, the molecular-level understanding of surface hybridization has not yet fully emerged and is therefore highly desired for designing an optimal surface hybridization protocol.

Gold has been extensively used to systematically study the interactions governing surface hybridization[13−18] due to its many useful properties as a model substrate.[19] However, hybridization on gold is affected by nonspecific adsorption of the exposed bases of ss-DNA.[20] Interestingly, the nonspecific DNA−gold interaction is found to be base-dependent, following the order A > G ≥ C ≫ T.[21] Typical probe sequences (15−30 nucleotides) at low surface densities ($\leq 5 \times 10^{12}$ cm^{-2}) exhibit hybridization efficiency of ≥60%[5,16,22,23] that is lower than what is observed in solution. A planar gold surface has been reported to significantly slow down[13] and lower free energy of hybridization.[24] AFM studies also suggested incomplete hybridization on gold.[25] Gold nanoparticles inhibit duplex formation of a random-coil DNA.[12] The duplex conformation of a hairpin DNA is also found to be destabilized on the gold nanoparticle.[12] It is likely that the

* Address correspondence to daspa@us.ibm.com and szafar@us.ibm.com.

Received for review April 27, 2015 and accepted June 7, 2015.

Published online June 08, 2015
10.1021/acsnano.5b02530

nonspecific interaction affects the conformational landscape in the close vicinity (≤1 nm range) of the gold surface. This effect would result in the modulation of the hybridization thermodynamics and kinetics, which remain still unexplored at the molecular level.

In this study, our goal is to understand the mechanistic details of hybridization on a planar gold surface and exploit that knowledge to design an improved surface for hybridization. Toward this goal, we have taken a unified approach of combing experiments with *in silico* molecular simulations performed on a 23 nucleotide probe DNA tethered to a gold surface. Sensing experiments show a conformational change of DNA accompanying hybridization occurring in close vicinity (~1 nm) of gold as well as conformational heterogeneity within hybridized DNA. Coarse-grained (CG) simulations of the system are consistent with experiments. Additionally, simulations indicate strong conformational heterogeneity on gold impedes hybridization, when compared to solution and to a repulsive surface. The molecular structure and population of those alternative populations are governed by the competition between specific base pairing and nonspecific interaction with gold. These results suggest that the hybridization efficiency can be enhanced by controlling conformational heterogeneity on the surface. Modulating surface chemistry at a nanometer length-scale by surface patterning with two dissimilar materials could be one possible way to achieve that goal. We performed simulations of the probe DNA tethered on gold dots of varying (2−8 nm) diameter patterned on a repulsive surface. A striking reduction of the conformational heterogeneity was observed on the 6 nm gold dot patterned surface, resulting in improved hybridization compared to the plain surfaces. Therefore, this study explores mechanistic details on the surface hybridization on gold and identifies a unique means to improve that by using a nanopatterned surface with an optimized patterning length.

RESULTS AND DISCUSSION

Real Time Probe Self-Assembly and Hybridization Measurements on Gold. The self-assembly and hybridization experiments of the 23 nucleotide long probe DNA on a gold surface were performed in real time using a recently proposed bipolar transitor based biosensor.[26] A key feature of this biosensor is its significantly higher resolution in comparison to other potentiometric biosensors such as nanowire field effect transitor sensors.[27−29] Hence, this biosensor is well suited for capturing details of a real time measurement curve.

Figure 1a shows the schematic of the bipolar junction transistor (BJT) based biosensor with gold as the sensing surface. The sensor consists of a BJT device with the base connected to the gold sensing surface immersed in phosphate buffer saline (PBS) solution; the AgCl/Ag reference electrode is used for applying

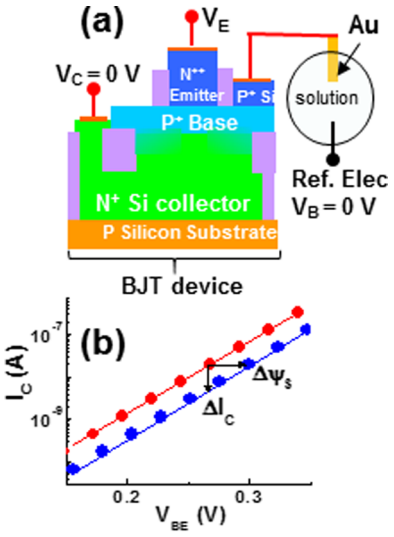

Figure 1. (a) Schematic of a bipolar junction transistor (BJT) based biosensor with gold as the sensing surface. (b) Measured dependence of the sensing current I_C on the applied voltage (V_{BE}) in 1× PBS solution; symbols are the measurements and solid line is the fit according to eq 1. Red curve was measured before the self-assembly of ss-DNA on gold sensing surface, and the blue curve was measured after the completion of self-assembly process. Post self-assembly, the curve was shifted by $\Delta\Psi_S$ toward higher voltage with an accompanying decrease in the sensing current by ΔI_C.

voltage to the solution. The sensing current is the collector current (I_C) and is given by the Ebers−Moll equation[30] as shown below:

$$I_C = I_o \cdot e^{q\cdot(V_B + \psi_S - V_E)/kT} \quad (1)$$

where, ψ_s is the gold surface potential, V_B and V_E are voltages applied at the base and emitter of the transistor, respectively. T is the temperature in Kelvin, k is the Boltzmann constant, I_o is a device constant, and q is the electronic charge. This equation implies that the sensing current I_C depends exponentially on the gold surface potential ψ_s. Since the surface potential depends on the charge density within the Debye length, changes in the charge density would cause exponential changes in the sensing current I_C. In other words, I_C can be used for sensing negatively charged DNA tethered to the sensing surface. Figure 1b shows the sensing current measured as a function of applied voltage $V_{BE} = (V_B - V_E)$ before and after incubation of the gold surface in 1× PBS solution with 0.5 μM of thiolated ss-DNA; measurement details are given in Methods section. Post incubation, I_C curve was observed to be shifted by $\Delta\psi_s$ toward higher voltage with a concomitant decrease of ΔI_C in the sensing current, thereby indicating that negatively charged ss-DNA had self-assembled on the gold sensing surface. Hence, I_C at a fixed applied voltage can be used for monitoring real time changes in the charge density associated with DNA molecules near the gold surface.

Figure 2a shows the sensing current (I_C) dependence on the incubation time during *in situ* self-

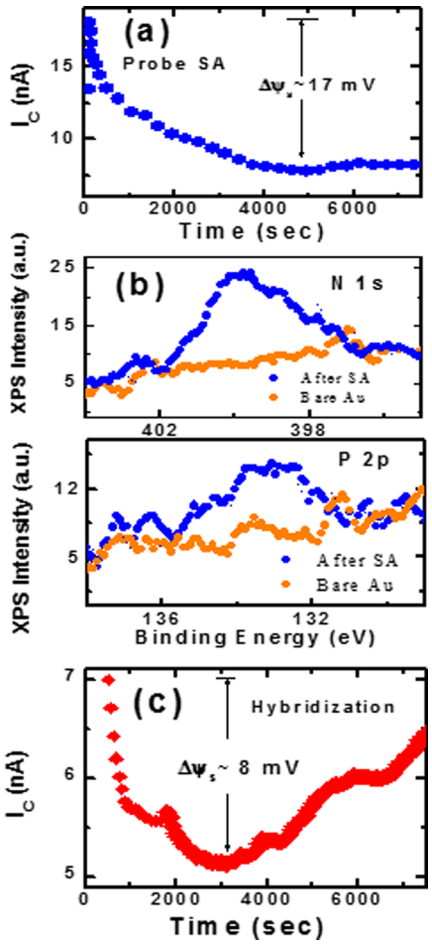

Figure 2. Real-time self-assembly and hybridization on gold. (a) Dependence of I_C on incubation time during the self-assembly (SA) of the thiolated probe ss-DNA on the gold sensing surface of the sensor; the self-assembly was initiated by adding 0.5 μM of probe ss-DNA to 1× PBS solution and I_C was measured at a constant V_{BE} = 0.264 V. (b) XPS spectra for bare gold surface and gold surface with self-assembled ss-DNA probes. (c) Dependence of I_C on the incubation time during hybridization of the self-assembled probe ss-DNA tethered to the gold surface; hybridization was initiated at time = 0 s by adding 1 μM of the c-DNA to 1× PBS solution and I_C was measured at V_{BE} = 0.264 V.

assembly of the probe ss-DNA on the gold surface. The self-assembly was initiated by addition of 0.5 μM probe DNA into a solution of 1× phosphate buffer solution (PBS) and was monitored by measuring the sensing current (I_C) at a fixed applied voltage of $V_{BE} = (V_B - B_E) =$ 0.264 V as a function of the incubation time. As shown in Figure 2a, I_C decreased with time and reached a steady state value after ~4000 s of incubation. This decrease is attributed to the self-assembly of the negatively charged ss-DNA probes over the gold surface. As the probes self-assembled, the negative charge density within the Debye length (~8 Å) increased and the surface potential (ψ_s) became increasingly negative. I_C was observed to decrease by a factor of ~2.3 which corresponds a surface potential change ($\Delta\psi_s$) ~17 mV as estimated from eq 1. In summary, Figure 2a indicates that the adsorbed probe DNA concentration increased with the incubation time before reaching a constant value, consistent with previous real time probe self-assembly studies.[5] To verify that the self-assembly of ss-DNA probes had occurred on the gold surface, the gold film was rinsed in 1× PBS solution after the completion of the self-assembly and XPS measurements were performed. Figure 2b shows the spectra measured before and after the self-assembly of the probe DNA on gold. The XPS spectra show nitrogen (N) and phosphorus (P) peaks for the self-assembled ss-DNA gold film and no peaks for the bare gold film. The observed peak positions are consistent with previously reported values for nitrogen and phosphorus.[31] The measured peak height N/P ratio is ~3.7, consistent with the predicted ratio of 3.6 for the probe DNA sequence used in the study. Hence, the measured XPS spectra confirm the self-assembly of probe ss-DNA on the gold surface.

Figure 2c shows the real time hybridization of the complementary DNA (c-DNA) with probe ss-DNA self-assembled on the gold sensing surface. Hybridization was initiated at time = 0 s by adding 1 μM of c-DNA to the 1× PBS solution. The real-time hybridization was monitored by measuring I_C at a constant V_{BE} = 0.264 V as a function of incubation time. Use of 1× PBS solution with a short Debye length of ~8 Å and a short linker length (see Methods) enabled us to investigate the charge density changes near (<1 nm) the gold surface during the hybridization process. The addition of c-DNA caused the sensing signal I_C to initially decrease with time and then to increase at longer incubation times (>3000 s). It should be noted that this I_C increase at longer times was not observed during the self-assembly of probe DNA (Figure 2a). We now discuss the physical interpretation of the measured I_C curve during the hybridization process. The observed decrease in I_C at shorter incubation time (<3000 s) indicates that the gold surface potential (ψ_s) was becoming increasingly negative. This ψ_s change is attributed to the adsorption of negatively charged c-DNA with some or all of its bases within 8 Å from the gold surface. At longer incubation times, the increase in I_C indicates a decrease in the negative charge density within 8 Å from the gold surface. This negative charge density decrease can be attributed two possibilities: desorption of DNA strands from the gold surface or the adsorbed DNA strands undergoing conformational change from a lateral orientation to a more vertical one with respect to the gold surface. To exclude the desorption possibility, XPS measurements were performed on two set of samples: gold surface with self-assembled probe ss-DNA and gold surface with hybridized DNA (see Methods). XPS spectra for both sets of samples remained unchanged after incubation (see Supporting Information Figure S1), thereby indicating desorption of probe DNA and hybridized duplex DNA from the gold surface were

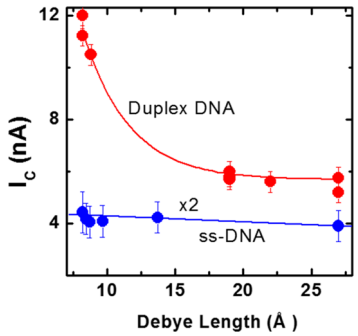

Figure 3. Dependence of the sensing current I_C measured at V_{BE} = 0.264 V on the Debye length for probe ss-DNA and hybridized duplex DNA tethered to the gold sensing surface. Debye length was varied by diluting the 1× PBS solution.

negligible during the real time hybridization measurements. Thus, we confirm that the observed increase in I_C at longer times was triggered by the conformational changes associated with duplex DNA formation, since duplex DNA is known to have more vertical conformation than ss-DNA with respect to the gold surface.[32−34] In summary, Figure 2c indicates that c-DNA was initially adsorbed in lateral conformations on the gold surface and after a lag of several minutes underwent conformational changes triggered by hybridization. Possible causes for this lag time can be a surface diffusion mediated search process of c-DNA for a tethered probe[4] and possible alternative populations[12,35] on the gold surface. In other words, hybridization with tethered ss-DNA did not occur directly from the solution but was mediated by the surface interaction.

Lastly, we compare the real time hybridization measurement of Figure 2c with those in the literature. Surface plasmon resonance spectroscopy (SPR) was used for measuring real time hybridization.[5] In contrast to the present study, the SPR study showed no signal reversal during the *in situ* hybridization. This discrepancy can be understood as follows: SPR is sensitive to total number of DNA molecules adsorbed on the gold surface, whereas the present sensing method is sensitive to both total adsorbed DNA molecules and their conformations within the Debye length.

Sensing Current Dependence on Debye Length for Probe and Duplex DNAs. To gain insights into ss-DNA and duplex DNA conformations with respect to the gold surface, sensing current I_C dependence on Debye length was investigated. Figure 3 shows measured I_C as a function of Debye length for probe ss-DNA and preformed duplex DNA self-assembled on gold surfaces (see Methods section); I_C was measured at a fixed applied voltage of V_{BE} = 0.264 V. Debye length was varied by varying the ionic concentration of the PBS solution from 137 to 14 mM; lower ionic concentration solutions were not used to minimize measurement errors due to the melting of duplex DNA. In Figure 3, I_C is observed to show no significant dependence on the Debye length for the probe ss-DNA, thereby indicating that ss-DNA were mostly laterally adsorbed within ∼8 Å of the gold surface. This observation of laterally adsorbed conformation is consistent with previous optical sensing studies on probe ss-DNA on gold surfaces.[12,34] In contrast, I_C sharply decreases as the Debye length increases from 8 to 18 Å and becomes almost constant for Debye length >18 Å for the tethered duplex DNA molecules. This I_C dependence implies that duplexes were confined within ∼18 Å from the gold surface. Previous studies have shown that duplex vertical distance from the tethering surface depends on several factors such as probe density,[36] surface potential,[33,34] and duplex flexibility,[32] and therefore, a direct comparison with literature values cannot be made. However, the present estimate of 18 Å is toward the lower end of the reported range of duplex DNA layer thickness, which likely suggest large conformational heterogeneity within the duplex population.

Probe Areal Density Estimation. We have also estimated the probe density from the measurements shown in Figures 2a and 3. I_C decreased by a factor of ∼2.3 corresponding to $(\Delta\psi_s) \sim 17$ mV as shown in Figure 2a. Using the solution double layer capacitance approximation, the surface charge density $(\Delta\sigma_s)$ can be written as $\Delta\sigma_s \sim (\Delta\psi_s)(\varepsilon\varepsilon_o/\lambda)$, where ε is the dielectric constant of the solution, ε_o is permittivity of vacuum and λ is the Debye length. Substituting $\Delta\psi_s \sim 17$ mV and $\lambda \sim 8$ Å, the probe related surface charge density $(\Delta\sigma_s) \sim 1.4 \times 10^{-6}$ C/cm^2. Since Figure 3 indicates that probe ss-DNA were laterally adsorbed within 8 Å of the gold surface, each probe DNA is estimated to have total charge of 23q. This charge estimation assumes the charge condensation effect to be negligible at 1× PBS for ss-DNA. Hence, the probe density is estimated to be $(\Delta\sigma_s)/23q = 4.3 \times 10^{11}$ cm^{-2}. This estimation of tethered probe density is consistent with previous studies.[5] For the estimated probe density of $\sim 4.3 \times 10^{11}$ cm^{-2}, the mean distance between two neighboring probes is ∼170 Å. Since this mean distance is greater than twice the fully stretched probe ss-DNA length, the present experimental results are valid for noninteracting probes.

In summary, these experiments (Figures 2 and 3) suggest an orientation change of DNA with respect to the gold surface during hybridization and also presence of significant conformational heterogeneity within the duplex population on gold. These results evoke a detailed modeling of the gold surface-mediated hybridization to gain a better mechanistic understanding.

Simulated Hybridization Landscape on Gold *vs* in Bulk and on a Repulsive Surface. We have performed extensive coarse-grained molecular dynamics simulations to investigate the DNA hybridization landscape on gold, which can be used in combination with the

experimental results to provide molecular insights onto this complex phenomenon. The probe sequence and the simulation conditions were kept identical to those in the sensing experiments within the framework of the simplified coarse-grained model (see Methods). Figure 4 shows a comparison of the PMF for hybridization (see Methods) on the model gold surface (blue) with that in bulk (black) and on a repulsive surface (red). The PMFs represent the reversible work done to bring the perfect complementary strand to the probe strand (free or surface-tethered) and hybridize. The low energy minimum at ξ = 13.5 Å corresponds to the perfectly hybridized state. The PMF is equal to zero, when the two strands are separated at ξ > 95 Å, as they do not interact. As they approach each other, the free energy in bulk increases due to the (i) charge−charge repulsion between the strand backbones, and (ii) the entropic penalty related to the relative alignment of the strands needed for hybridization. The effect of the repulsive surface on the PMF profile is minimal. At distances 20 Å < ξ < 50 Å, the free energy barrier on the repulsive surface becomes slightly higher than that in the bulk due to the restricted approach of the target strand. The available conformational space in which the two strands start to align to form a duplex is reduced due to the excluded volume interaction of the surface. The presence of surface slightly destabilizes the hybridized duplex, as suggested by the $\Delta\Delta G^{\text{Surface}}_{\xi=13.5 \text{ Å}}$ = 0.9 ± 0.5 kcal/mol.

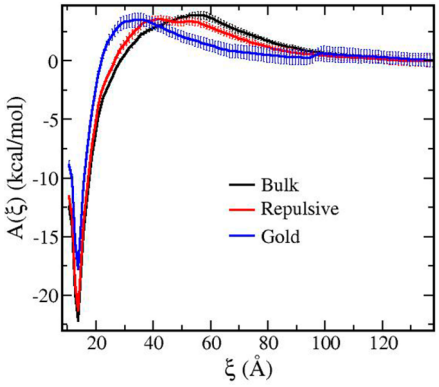

Figure 4. 1D Potential of mean force (PMF, in kcal/mol) of hybridization. The reaction coordinate ξ is defined as the center-to-center distance (Å) between the probe and target strands. Data for bulk, repulsive surface, and gold surface simulations at [*I*] = 130 mM are shown in black, red, and blue, respectively. Data plotted are the averages and standard deviations obtained from at least three different ~150 ns runs for each system.

The presence of the gold surface significantly alters the PMF of hybridization. The free energy at the distant regime (40 Å < ξ < 95 Å) is considerably reduced on gold, suggesting that gold surface favors approaching of the two strands to each other. For example,

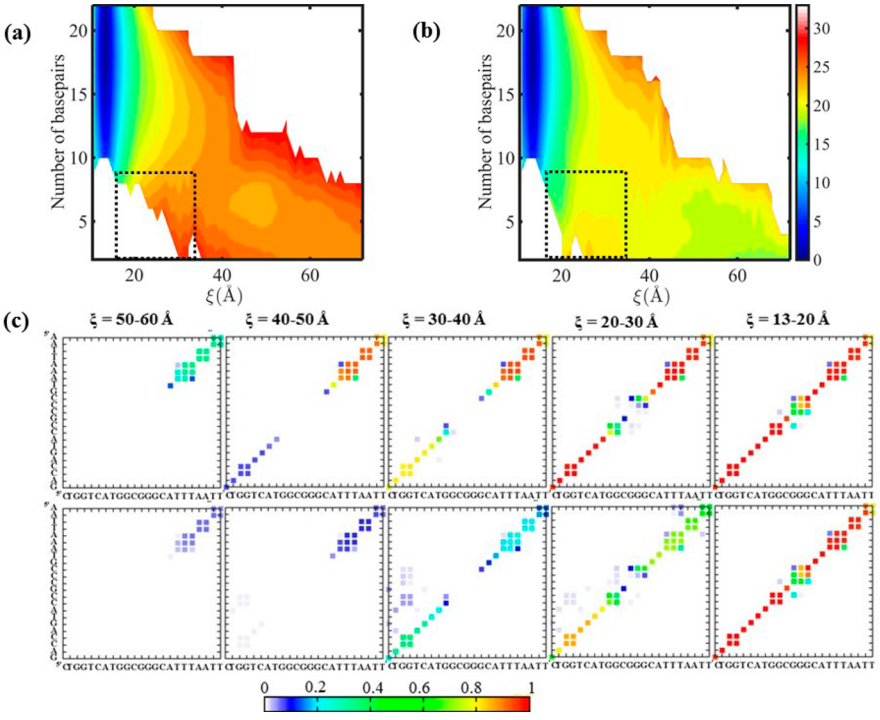

Figure 5. Hybridization pathway on gold and on the repulsive surface. (a and b) 2D PMF (in kcal/mol) as a function of probe-target distance, ξ, and number of base pairs for hybridization on the repulsive surface (a) and on the gold surface (b). Each contour represents 1.0 kcal/mol free energy difference. Black dotted rectangle corresponds to the partially hybridized configurations populated on gold (shown in yellow) when the strands are within 30 Å. Color-scale used is shown at right. (c) Ensemble-averaged contact maps for different stages of hybridization (different windows of ξ) on surface: repulsive (top) and gold (bottom). The sequences for the probe (*x* axis) and the target (*y* axis) are also shown. The top right and bottom left corners of the contact maps correspond to the free and the tethered ends of the probe, respectively. The contacts are colored according to the normalized probabilities using the color scale shown at bottom.

$\Delta\Delta G^{Gold}_{\xi=55\ Å}$ with respect to bulk is -2.4 ± 0.6 kcal/mol. The PMF starts to increase on gold, as the two strands start to align at $\xi < 60$ Å. Thus, the PMF barrier is positioned at much closer distance compared to in bulk and on the repulsive surface. We also find that the gold surface considerably lowers the duplex stability, when compared to bulk, by $\Delta\Delta G^{Gold}_{\xi=13.5\ Å} = 4.4 \pm 0.6$ kcal/mol.

Presence of Partially Hybridized States on Gold. Figure 5a,b shows the two-dimensional PMFs on the repulsive surface, and on gold as a function of ξ and the number of base pairs formed. In addition, we also compare the conformational ensembles populated at different windows of ξ. For this purpose, the averaged contact probabilities for all possible base pairs were estimated and presented as contact maps in Figure 5c (see Methods). Combining the 2D PMF plots with these contact maps offers detailed structural insights along the hybridization reaction in a different environment. Results for the hybridization in bulk is shown in Supporting Information (Figure S3). Data up to $\xi = 72.5$ Å was considered for these 2D PMFs, as base pair formation is negligible and the 1D PMFs resemble each other beyond that distance (Figure 4).

Overall, the hybridization in bulk appears downhill, which is initiated by a nucleation event at 50 Å $< \xi <$ 60 Å (Supporting Information Figure S3), in which in-register base pair forms at either end, with a preference for the 5′ end in the present case due to higher GC content of this region. As ξ decreases, the strands form hybridized antiparallel duplex. A bubble in the middle is often seen. Only, a few non-native contacts (off-diagonal contacts) are found near the center region due to presence of short palindromic tracts. Whereas the 2D PMF on the repulsive surface (Figure 5a) closely resembles the one in bulk, the initial base pairing at the free end of the probe is favored (see Figure 4c, contact map at 40 Å $< \xi <$ 50 Å) due to the excluded volume interaction with the surface. This effect causes a shallow basin representing conformations with the free end hybridized (Figure 5a).

In sharp contrast, hybridization on gold is not a simple downhill process. The uncomplexed and some partially hybridized structures (0−8 base pairs formed) at $\xi > 45$ Å are stabilized on gold (Figure 5b). The contact map consistently shows only some weak contact formation at the free end of the probe at $\xi > 40$ Å (Figure 5c). There also exists a free energy barrier at 25 Å$< \xi <$ 45 Å, implying that gold restricts further approach of the two strands. At this stage, preferential contact formation at the tethered end of the probe is seen, which is opposite to the repulsive surface scenario. A few non-native contacts are also observed. Comparing the contact maps on gold with those in bulk and on the repulsive surface, it is evident that gold impedes full hybridization and stabilizes partial duplexes. Interestingly, a significant population of partially hybridized

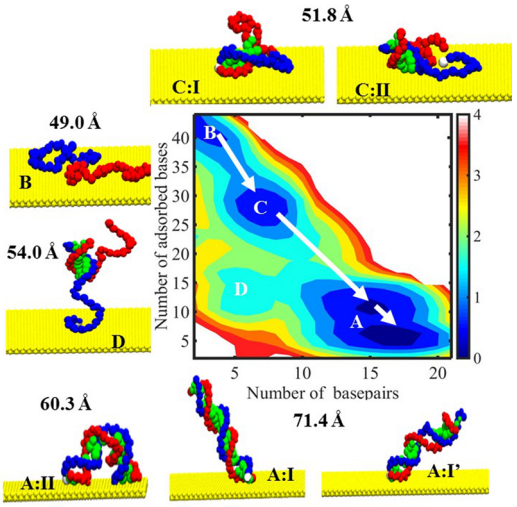

Figure 6. 2D free energy landscape (in kcal/mol) as a function of the number of base pairs (*x*-axis) formed and the total (probe + target) number of adsorbed bases estimated from the conformations sampled during hybridization. Each contour represents 0.5 kcal/mol free energy difference (color-scale shown on right). A base was considered adsorbed, if it was found within 8 Å of the surface. Representative configurations for the highly populated regions are also shown. The probe backbone is shown in blue, while the target backbone in red. Bases (in green) are only shown if they form a contact. Tethered site is shown in white. The green arrows show the hybridization pathway (as a function of ξ). The average end-to-end distance for the target strand is also reported for the main states.

structures (∼8 base pairs) at close distance (15 Å $< \xi <$ 30 Å, black rectangle, Figure 5b) is found on gold, which is not seen either in bulk or on the repulsive surface. These findings reveal higher conformational heterogeneity during hybridization on gold.

Surface Adsorption Favors Partial Duplex and Bent, Full Duplex. To estimate the influence of nonspecific interactions on the conformational heterogeneity, we compute the 2D free energy landscape as a function of the number of base pairs formed and the number of adsorbed bases on gold from all conformations populated along the hybridization pathway (Figure 6). This analysis reveals that there exist several distinct populations along the hybridization pathway, which differ from each other with respect to the degrees of base pairing and adsorption. Significant variability is observed even within the fully hybridized state (state A, ≥70% hybridized). Structures from the A-state with low adsorption (≤7 bases adsorbed) are either fully hybridized (structure A:I) or have a bubble in the middle (structure A:I′). Those structures show an average tilt angle of ∼47° (see Supporting Information). A significant population of duplex structures with bubble frequently interact with gold at the free end, resulting in bent duplexes (structure A:II).

The strongly adsorbed conformations populated during hybridization can be classified in two separate states (states B and C). Very few base pairs are formed in the state B, suggesting configurations comprising

uncomplexed strands (*i.e.*, larger ξ) that are mostly adsorbed. The average end-to-end distance of 49 Å for this state implies compact coil structures. This state represents the end-state of the 2D search process of the surface-bound target to the probe,[4] corresponding to the lower PMF at 40 Å < ξ < 72 Å (see Figure 4). As the strands get closer, a strongly adsorbed and partially hybridized state (state C) with ~6−8 base pairing interactions are formed. A more favored nucleation at the GC-rich tethered end in this C-state (Figure 5c) allows nonspecific binding of the A-rich free end (structure C:I). However, some structures with free end (structure C:II) or both ends involved in base pairing can be also present in the C state. A much less populated state D composed of weakly adsorbed, partially hybridized configurations is also seen, indicating a minor fraction of hybridization events happening from solution, as opposed to on the surface.

Comparison of Simulations with Experiments. We commence by comparing simulations with the experimental results of Figures 2 and 3. It should be mentioned that the REUS technique used here does not provide any information on the time-scale of hybridization in different environments. The simulations of this study offer molecular details of the hybridization pathway and PMF of hybridization. Thus, the PMFs and the conformations populated along the process can be compared to explore the effect of environment (solution *vs* surface, *etc.*) on hybridization efficiency and pathway. The simulated conformational changes of DNA with respect to the surface can be also directly compared with experiments. Figure 2 indicates that target DNA is first laterally adsorbed on the gold surface and then undergoes hybridization with lateral-to-vertical conformational changes. The simulations (Figure 6) consistently reveal nonspecific adsorption of the target strand facilitating the approach to the surface-adsorbed probe, resulting in state B. Next, a metastable state compriong of the surface-adsorbed, partial duplexes is populated (state C). Thus, the time delay preceding the current inversion in experiments likely includes the simulated B and C states. The transformation of the C state to A state (structures I, I′, and II) accompanying desorption elucidates the current inversion. It should be noted that both experimental (Figure 2) and simulation (Figure 6) hybridization results correspond to 8 Å Debye length from the gold surface. In contrast, simulated hybridization on a repulsive surface was found to occur directly from solution, consistent with recent single-molecule FRET experiments.[35]

Figure 7 shows the simulated change in the DNA charge density as a function of the vertical distance from the gold surface. When only state A (Figure 6) is considered in this calculation, ~50% of the charge density (black curve) was found to reside within 20 Å from the surface. If we include the surface-adsorbed,

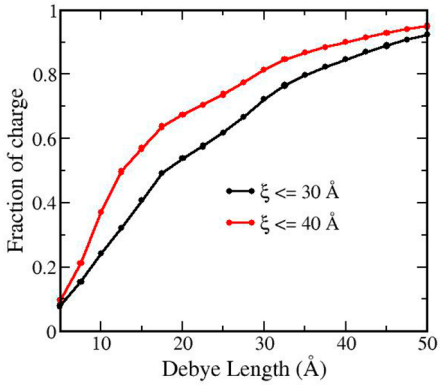

Figure 7. Charge density change as a function of vertical distance (equivalent to Debye length in Figure 2) from the gold surface. The conformations populated at ξ < 30 Å (in black) and ξ < 40 Å (in red) are considered for this calculation.

partial duplexes (state C, Figure 6), ~70% of the charge density (red curve) is located within 20 Å. The slope of those curves further suggests that the rate at which the charge density of those populations decreases with increasing Debye length becomes slower after 20 Å. A linear fit of the black curve suggest that the slope is ~0.33 for the Debye length ≤20 Å and then decreases to ~0.012. These simulated results agree well with experimental observations, which indicates that most of the duplex is confined within 20 Å from the gold surface (Figure 3).

Simulations also provide insights into how the conformational heterogeneity present within the duplex conformation can account for the observations in Figures 3 and 7. The presence of small bubbles in ds-DNA (states A:I′ and A:II, Figure 6) observed in simulations is reported at physiological temperature.[37−39] Such bubble can result in lowered bending stiffness compared to the double helix one at shorter length-scale, while still keeping their long length behavior consistent with the worm-like-chain model. Our simulations reveal that those more flexible duplexes frequently interact with gold at the free end of the probe (structure A:II), where some fraying is seen. The PMF analysis implies that those surface-adsorbed bent duplexes stay in equilibrium with the full duplex (Figure 4-5). Similar bent DNA duplexes has been experimentally reported for 20 nucleotide DNA immobilized on gold with a short linker.[32] Those bent duplexes account for the observed higher charge density on surface, compared to what is expected for a minimally adsorbed duplex with an average ~47° tilt angle (structure A:I and A:I′, Figure 6). Presence of some surface-adsorbed, partial duplexes on gold (C state, Figure 6) can further contribute to the small layer thickness observed experimentally (Figure 3).

Next, we compare the simulation results with literature. Simulations (Figures 4 and 5) imply impeded hybridization and lowered duplex stability on gold, consistent with several previous experiments.[12,13,24,25,6]

The metastable intermediate state comprising partial duplexes on gold detected in simulations (Figure 6) is consistent with experimental prediction based on hybridization-induced fluorescence change of DNA attached to gold nanoparticle.[12] These partial duplexes likely account for the experimentally observed population with lower T_m on gold.[12] The present modeling (Figures 5c and 6) also reveals the molecular structure of these partial duplexes, which is governed by the competition between specific base pairing and nonspecific attraction with gold. The use of a spacer (linker) between the gold surface and the probe sequence will help reducing this competition to some extent (see ref 40 and references therein). The commonly used linkers are either inert (*e.g.* hexamine) or polynucleotide (polyT preferred due to its lower preference for gold) in nature. If the spacer results in less interaction with gold surface, we would expect the experimental results of Figure 3 to be modified: the curve is expected to saturate at longer Debye length. The simulated PMF of hybridization on gold (Figure 4) will exhibit a smaller barrier and enhanced duplex stability in that case, when compared to what are observed without spacer. Another benefit of using a linker is lowering of the steric hindrance of the probe due to presence of the solid surface. However, the surface-assisted approach of two strands on gold might suffer due to the presence of a linker. Use of a polynucleotide spacer may further facilitate formation of non-native interactions depending on the probe sequence, which will result in impeded hybridization. The competition between the specific and nonspecific interactions also depends on the probe sequence. For example, an AT-rich sequence suffers from higher competition (thus more impeded hybridization on gold) compared to a GC-rich sequence of same length due to the base-dependent nature of the nonspecific interaction. The nucleotide distribution within the sequence can affect hybridization landscape on gold as well. Future studies will be directed to quantify the effect of probe sequence, probe length, linker chemistry, and linker length on hybridization on gold.

Hybridization on a Nanopatterned Surface of Two Dissimilar Materials. The overall agreement of the simulations with present sensing experiments and other published experimental data encourages us to exploit this *in silico* model of DNA on gold toward designing an improved surface hybridization protocol. Simulation results reveal that the nonspecific binding with gold facilitates the approach of two strands at the earlier stage of hybridization (40 Å< ξ < 72 Å). However, the alternative populations resulting from nonspecific binding with at the late stage (when strands are close, *i.e.* ξ < 40 Å) impedes hybridization. Therefore, one way to achieve a better surface for hybridization is to tune the surface chemistry in a length-scale dependent manner, such that the conformational heterogeneity would be reduced, while still favoring the approach.

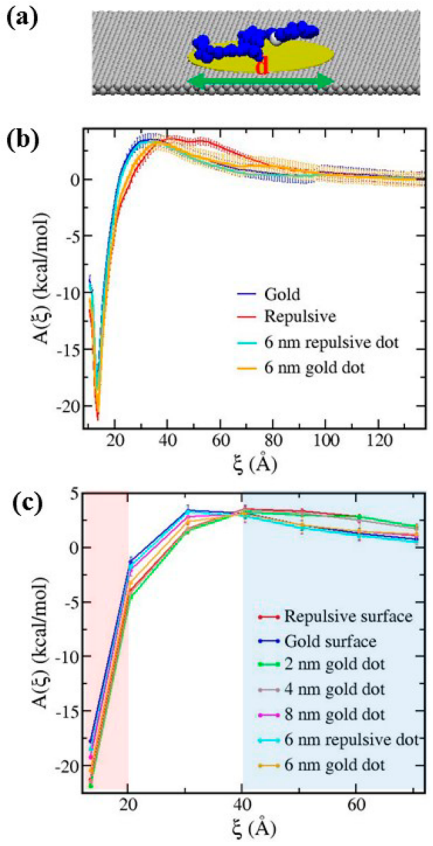

Figure 8. Hybridization on a nanopatterned surface. (a) A tethered probe (in blue VDW spheres) on a gold nanodot with diameter of *d* nm (in yellow) patterned on a repulsive surface (in gray). (b) 1D PMF plots as a function of ξ on the two nanopatterned surfaces with 6 nm nanodots: gold nanodot on repulsive surface (in yellow) and repulsive nanodot on gold surface (in cyan). Data for plain repulsive and gold surfaces are also shown for comparison red and blue, respectively. (c) The effect of nanodot size on PMF of hybridization. For clarity, only data for discrete values of ξ are shown (see also Supporting Information Figure S4). Different color shading has been used to highlight the change in PMF of the 6 nm gold dot patterned repulsive surface as a function of ξ.

Nanopatterned surfaces made of two dissimilar materials in terms of the nonspecific binding, such as a combination of gold (attractive) and a repulsive material (*e.g.*, epoxy/amine-treated SiO_2), are investigated *in silico* for this purpose. Hybridization is simulated on two different nanopatterned surfaces: (1) a gold nanodot on a repulsive surface (see Figure 8a), and (2) a repulsive nanodot on a gold surface. The probe is immobilized on the nanodot in these simulations (see Methods). Most of the species contributing to the structural heterogeneity (mainly partially hybridized C state and bent, full duplex A:II structures) have an average end-to-end distance between ~50 and ~60 Å (see Figure 5). The end-to-end distance distribution plot (Supporting Information Figure S4) consistently shows higher probability of C and A:II

structures with an end-to-end distance ranging between 50 and 65 Å. The bent duplex corresponds to a narrower distribution with a much shorter tail at low end-to-end distance values, when compared to the C-state. Supporting Information Figure S4 clearly suggests that the nanodots with radius ≤40 Å can improve hybridization by not accommodating most of the C and A:II structures. Therefore, nanodots of 2, 4, 6, and 8 nm in diameter were simulated to examine the effect of the length-scale of a nanopatterned surface on the hybridization.

Figure 8b and Supporting Information Figure S5 demonstrate the 1D PMF of hybridization on those nanopatterned surfaces. Interestingly, the hybridization on the 2 and 4 nm gold nanodots closely follows the trend of the bulk surface (Supporting Information Figure S5). Thus, 2−4 nm sized nanodots appear to be too small to affect hybridization. In contrast, the PMF for hybridization on the 6 nm gold nanodot shows an interesting pattern (Figure 8b). Beyond ∼80 Å, the PMF is similar to the one on a plain repulsive surface. At 40 Å < ξ < 70 Å, hybridization follows the trend observed on a plain gold surface. At shorter distance, the PMF again appears similar to what is seen on the plain repulsive surface. The larger 8 nm gold nanodot patterned surface shows a similar pattern; however, the PMF starts to mimic the one seen on the plain gold surface.

In contrast, hybridization on the gold surface patterned with different sized repulsive nanodots consistently appears to follow the trend seen on the plain gold surface (Figure 8b,c and Supporting Information Figure S5), implying that the bulk gold surface still controls hybridization. These results are further summarized in Figure 8c, which reveals an optimal hybridization performance of the 6 nm gold nanodot patterned surface with respect to plain surfaces (gold and repulsive). In that case, the approach of target strand to the probe is favored at 40 Å < ξ < 70 Å (blue shaded region, Figure 8c), as seen on plain gold, whereas at smaller distance, the barrier is lower (white shaded region, Figure 8c). The duplex is found to be stabilized similar to the one on the plain repulsive surface (pink region). Thus, our simulations reveal a striking improvement of surface hybridization on a 6 nm gold nanodot patterned repulsive surface, which is clearly governed by the length-scale of the nonspecific attraction.

The effect of the nanopatterned surface with 6 nm gold dot on hybridization is further evident from Figure 9a. The uncomplexed and partially hybridized structures at ξ > 20 Å (see Figure 5b) are less populated on this nanopatterned surface, when compared to gold; however, the population remains still higher compared to what is seen on the plain repulsive surface. Figure 9b consistently reveals strikingly lower population of the surface-adsorbed structures (both B and C states) during hybridization compared to what seen on plain

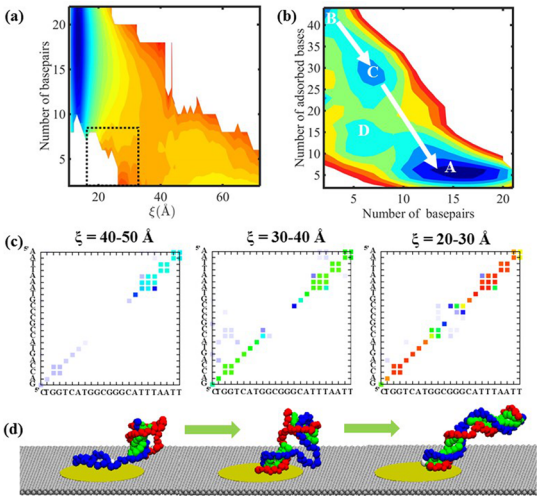

Figure 9. Hybridization on the repulsive surface patterned with 6 nm gold dots. (a) 2D PMF (in kcal/mol) as a function of ξ, and number of base pairs, and (b) 2D free energy landscape (in kcal/mol) as a function of the number of base pairs formed and the total number of adsorbed bases estimated from the conformations sampled during hybridization. (c) Ensemble-averaged contact maps for different stages of hybridization (different windows of ξ). (d) Representative configuration at different stages of hybridization. Color-scales used are same as in Figures 5 and 6.

gold. Interestingly, the subpopulation within the A state that experience higher adsorption (*i.e.*, A:II, bent duplex with a bubble) on plain gold has also disappeared. Thus, the conformational heterogeneity on this nanopatterned surface appears much lower compared to what seen on a plain gold surface. At the same time, there is some population of the surface-bound structures at larger probe−target distance (40 Å < ξ < 60 Å) that facilitates the approach of two strands. Consequently, the PMF barrier for hybridization on this nanopatterned surface becomes lower compared to both plain gold and plain repulsive surfaces, while the fully hybridized duplex gains stability similar to what seen on the plain repulsive surface (Figure 8b).

The contact maps for (Figure 9c) reveal that, as the strands approach closer (40 Å < ξ < 50 Å), the initial nucleation preferably occurs at the free end of the probe. The representative structure shows that probe at this stage lies mostly flat on the gold nanodot in order to maximize nonspecific binding, whereas the target approaches from solution (Figure 9d). As the free end of the probe has higher chance to stay outside of the nanodot, initial nucleation occurs at the free end. At a later stage (30 Å < ξ < 40 Å), the C state conformations with a ∼8 bp bubble at the center form, as the target tries to move inside the gold nanodot due to nonspecific attraction (Figure 9c,d). This scenario is distinct from what is seen on plain gold (preferred nucleation at the tethered end of probe) and on the plain repulsive surface (preferred nucleation at the free site of the probe) at this stage of hybridization

(Figure 5c). A few non-native contacts near the tethered site are also observed. In those structures (Figure 5d), the region near the bubble still interacts with gold. It appears that desorption of those structures accompanying closure of the bubble is more favorable compared to the scenario on the plain gold, in which the strongly adsorbed, partial duplexes need to desorb prior to further hybridization. Consequently, the PMF at 30 Å $< \xi <$ 40 Å is lower than what is estimated on plain gold and fully hybridized A state starts to appear earlier (20 Å$< \xi <$ 30 Å) on this nanopatterned surface.

Taken together, these results imply that the 6 nm gold nanodot restricts the occupied volume of the surface-adsorbed conformations. Such effective nanoconfinement promotes approach of strands compared to what is seen on the repulsive surface. The PMF barrier arising from the strand alignment and charge−charge repulsion is thus overcome by the nonspecific attraction. At the same time, the size of the nanodot hinders stabilization of the surface-adsorbed duplexes. As a result, base pairing at both ends is promoted, while a bubble at the center can interact with gold. Finally, desorption of this bubble leads to full hybridization. Consequently, PMF barrier is lower compared to both plain gold and plain repulsive surfaces.

In summary, a gold dot of 6 nm diameter on the repulsive surface appears to provide optimal hybridization by lowering the alternative state populations, while still favoring approach of the two strands for the 23 nucleotide DNA studied here. The present estimate of 6 nm as the optimal patterning length depends on two distinct molecular factors: (1) the physical size of the partial and bent duplexes stabilized by nonspecific interactions (Supporting Information Figure S4), and (2) the available gold surface area of the 2D nanoconfinement that facilitates further zippering after initial hybridization (Figure 8d). As a result, a smaller 2−4 nm or a larger 8 nm gold nanodot cannot induce similar effects as observed in the case of the 6 nm gold dot.

The optimal patterning length will definitely scale up with probe length. As the physical size and population of the C and A:II states will also vary with DNA sequence, we expect the optimal nanodot size to have some sequence dependence as well. Nevertheless, the repulsive surface patterned with gold nanodots should assist hybridization in general. In practice, such nanopatterned surface can be prepared by high resolution nanopatterning techniques such as e-beam lithography,[41] nanoimprinting,[42] or directed self-assembly of block copolymers.[43,44]

CONCLUSIONS

We have combined real-time hybridization experiments performed using a bipolar transistor based biosensor with extensive coarse-grained molecular simulations to examine the effects of the gold surface chemistry on the hybridization pathway of a surface-tethered 23 nucleotide probe DNA. The sensing experiments indicate a lateral-to-vertical orientation change of DNA upon hybridization and a significant heterogeneity within the duplex DNA population on gold. Simulations are consistent with experiments, while providing detailed structural insights onto the distinct alternative populations along the reaction. A partially hybridized, strongly adsorbed, metastable intermediate is detected on gold during hybridization. At a much later stage, bent duplexes with a bubble at the center stay in equilibrium with the straight duplex. These alternative populations contribute to the impeded hybridization and lowered duplex stability on gold. On the basis of these mechanistic insights, we further provide a novel method for improving the surface hybridization by using a nanopatterned surface of two dissimilar materials. Simulations were performed on the probe tethered on gold dots of varying (2−8 nm) diameter patterned on a repulsive surface. A striking improvement in hybridization for the 6 nm diameter gold dot was revealed compared to plain surfaces. The 2D nanoconfinement provided by the 6 nm gold dot favors the approach of two strands and at the same time reduces conformational heterogeneity for the present probe. Thus, improved DNA hybridization can be achieved on gold nanodot patterned repulsive surface, where the optimal dot diameter will depend on the probe length and sequence. In summary, this study provides mechanistic insights onto surface hybridization and offers a unique approach for improving that by using a nanopatterned surface with an optimized patterning length.

METHODS

Experimental Details. *Materials and Self-Assembly Procedures.* We used a 5′ dithiol-modified (DTPA) 23 nucleotide long sequence (CTGGTCATGGCGGGCATTTAATT) as the probe single strand DNA (ss-DNA). All experiments were performed in 1× PBS (Sigma-Aldrich) and room temperature, unless otherwise stated. The 1× phosphate buffer solution (PBS) solution was diluted with nucleus free water to prepare PBS solutions of varying concentrations, whenever needed. These probe ss-DNA were self-assembled on gold film surfaces. The gold films of 100 nm thickness were sputter deposited on silicon substrate with 10 nm thick chromium as the adhesion layer between gold and silicon substrate. Before the self-assembly process, the gold surfaces were cleaned by soaking them in ethyl alcohol (200 proof) for 10 min. The self-assembly of probe ss-DNA on the gold surface was performed by incubating in 1× PBS solution with 0.5 μM of ss-DNA for ∼2 h; the gold film was rinsed in 1× PBS solution for 3 min after the completion of self-assembly. Hybridization was performed by incubating the gold film with self- assembled probes ss-DNA in 1× PBS solution with 1 μM of complementary DNA (c-DNA) for 2 h; the gold film was rinsed in 1× PBS solution for 3 min after the completion of hybridization.

Preformed duplex DNA were also self-assembled on gold surfaces as follows. Duplex DNA were formed by mixing 0.5 μM concentration each of probe DNA and c-DNA in 1× PBS solution. After mixing probe and c-DNA, the PBS solution was first heated to 80 °C for 5 min and then cooled to room temperature over about 3 h. The cooled solution was stored at 4 °C overnight before being used for self-assembly of preformed duplex DNA. A cleaned gold film was incubated in the solution with preformed duplex DNA for 2 h; the gold film was rinsed for about 3 min in 1× PBS solution after the completion of self-assembly of duplex.

Electrical Measurements. A bipolar transistor based sensor[26] was used for measuring self-assembly and hybridization. The sensor consists of commercially available bipolar junction transistor device (NPN-2N2222A) with its base connected to a gold sensing surface. The reference electrode used was AgCl/Ag electrode (Innovative Instruments, Inc., Tampa, Florida) with outer diameter of 1 mm. The electrical sensing measurements were performed as follows. The collector current (I_C) was the sensing signal. The voltages applied at the emitter, collector, and AgCl/Ag reference electrode were V_E, V_C, and V_B, respectively. Sensing measurements were made with $V_C = V_B = 0$ V , while V_E was either varied or set at a fixed value. The electric measurements were made using source measurement unit (SMU) Agilient B1500.

XPS Measurements. X-ray photoelectron spectroscopy (XPS) spectra were acquired using a commercial XPS with a monochromatic Al Kα source. The reported binding energies were based on the analyzer energy calibration (Au 4f measured at 83.9 eV for all samples). For each spectrum, the total number of scan was set to 40, spot diameter was 300 μm and step size was 0.1 eV/point. Samples used in XPS studies were first rinsed in 1× PBS solution and dried in N_2 flow and then loaded in the spectrometer.

Simulation Model and Setups. *Coarse-Grained (CG) DNA Model.* In this study, we have used the 3SPN.2 CG DNA model that has been recently developed by Hinckley and co-workers (see Supporting Information).[23] In this model, the bonded and nonbonded potentials are constructed to penalize deviations from the B-DNA crystal structure. Bond, angle, and dihedral potentials are sequence-independent, while base-stacking energies and base pairing energies depend on the sequence and use anisotropic potential. The charged phosphate sites of the DNA interact *via* a screened electrostatic potential. The model parameters have been shown to correctly reproduce the experimentally measured structural properties, persistence lengths, melting temperatures, and hybridization rate constants.[45,46] In particular, the model accurately describes molecular flexibility for both ss-DNA and ds-DNA, which is important for characterizing the conformational landscape of hybridization.

Model of Gold Surface. The gold surface was modeled with a flat wall positioned at $z = z_{min}$, which interacts with the DNA strands with 12−6 Lennard−Jones potential $U_{gold} = 4\varepsilon[(\sigma_{sur}/r_{sur})^{12} - (\sigma_{sur}/r_{sur})^{6}]$, with a cutoff distance $r_c = 12$ Å. The values of σ_{sur} were site-specific and were derived using the combination rule $\sigma_{sur} = 1/2(\sigma_{gold} + \sigma_i)$, where $\sigma_{gold} = 2.6$ Å and σ_i is the VDW diameter of a particular site i used in 3SPN.2 model. The interaction strengths were site-dependent and were set to $\varepsilon_{Phosphate\text{-}surface} = 0.24$ kcal/mol, $\varepsilon_{Sugar\text{-}surface} = 0.1$ kcal/mol, $\varepsilon_{A\text{-}surface} = 4.0$ kcal/mol, $\varepsilon_{G\text{-}surface} = \varepsilon_{C\text{-}surface} = 2.0$ kcal/mol, and $\varepsilon_{T\text{-}surface} = 1.0$ kcal/mol. Those interaction parameters were designed to mimic the base-dependent gold−DNA interactions observed in experiments, suggesting the order A > G ∼ C > T.[21] A lower gold affinity of the ds-DNA has been also reported compared to the ss-DNA, due to the sequestration of the reactive bases.[20,21,47] Experiments also suggested that the high affinity of oligo(dA) for gold can inhibit the expected hybridization of an A + T mixture at room temperature; however, the G + T mixture formed hybrids on gold.[21] To take into account such effect in our model, we set $\varepsilon_{A\text{-}surface} = \varepsilon_{A\text{-}T} = 4.0$ kcal/mol, such that the A-gold interaction can efficiently compete with A-T base pairing. The DNA−gold interaction parameters were further verified by estimating the effect of the gold surface on the melting temperature and tilt angle (see Supporting Information).

Model of Repulsive Surface. The repulsive surface was modeled with a Weeks−Chandler−Anderson potential that mainly acts as an excluded volume potential and is therefore entropic in nature. The potential has the form $U_{repulsive} = 4\varepsilon[(\sigma_{sur}/r_{sur})^{12} - (\sigma_{sur}/r_{sur})^{6}] + \varepsilon$, where ε is set to 0.05 kcal/mol, r_{sur} is the distance between a particular base and the surface. The values of σ_{sur} were the same used as in the gold case. The potential falls smoothly to zero at $r_c = 2^{1/6}\sigma_{sur}$.

Model of Nanopatterned Surface. The nanopatterned surfaces were designed *in silico* by placing a circular nanodot of the desired chemistry and size on the bulk surface. Within and outside the nanodot, the surface−DNA interaction was modeled by the potential used for the corresponding plain surfaces.

Simulation Setup. Periodic boundary condition was imposed in all three directions for the bulk simulation and only in the *xy* plane for the simulations on the surface. The box size for all simulations was 135 × 135 × 265 Å^3. To prevent escape of the atoms from the box in simulations on an attractive or a repulsive surface, a flat wall fixed at $z = z_{max}$ was placed, which interacts with the DNA strands with a 12−6 Lennard−Jones potential with ε = 0.05 kcal/mol and r_c = 12 Å. A Langevin dynamics integration scheme with a time step of 0.02 ps was used in all simulations. All simulations were run using the USER-3SPN2 package implemented within the LAMMPS software.[48]

The simulation conditions were chosen to mimic the experiments as close as possible within the simplified framework of the model. The *x* and *y* dimensions of the simulation box were set to 135 Å to mimic the low probe density in experiments. The 5′ end (the sugar bead) of the probe DNA was tethered at 6 Å from the surface by applying a spring force with a force constant of 2 kcal/Å to mimic the probe tethering via a short linker in experiments. The ionic strength was set to 130 mM (equivalent to 1× PBS buffer).

Replica Exchange Umbrella Sampling (REUS) Simulations. At least three independent 150 ns long REUS[49,50] simulations (initialized with different velocities) were performed for each system at 300 K in the NVT ensemble using a Langevin thermostat. The center-to-center distance between the two strands, ξ, was used as the reaction coordinate, ranging between 10 and 138 Å in increments of 0.25 Å, resulting in total 512 replicas. This equals to ∼230 μs simulation time per system, resulting in an aggregate of ∼2600 μs simulation time used in this study. A biasing potential was applied to every replica, which was of the form $U^i_\xi = K_\xi (\xi - \xi_0)^2$, where K_ξ equals to 12 kcal/(mol/Å^2), ξ_0 is the equilibrium distance between the strands for the particular replica, and ξ is the instantaneous distance. The initial replica structure was generated by a pulling simulation starting from the B-DNA structure. Each replica was first equilibrated from 1 ns. Exchanges were attempted every 20 ps.

Potential of Mean Force (PMF) Calculation. PMF for hybridization was calculated by using the weighted histogram analysis method (WHAM).[51] Results from different REUS runs were used in the average and standard error estimation for PMF. First 10 ns of the REUS trajectory were not used for analysis.

Simulation Analysis. A base was considered adsorbed, if it was found within 8 Å of the surface. The number of formed base pair used in the PMF calculation was estimated as following: A base pair is defined, if that particular base pairing interaction energy estimated during the simulation is at least 80% of the maximum possible energy. For the contact map computation, a distance-based criterion was used, in which a contact between two bases was considered to be formed, if the two complementary bases were within σ_{ij} + 2 Å.

Conflict of Interest: The authors declare no competing financial interest.

Acknowledgment. P.D. thanks Blue Gene Science program for support and D. Hinckley for helpful advice on the use of 3SPN.2 DNA model. S.Z. would like to gratefully thank Professor M. Levy from Albert Einstein Medical School, Bronx, NY for graciously providing nucleotide single strands.

Supporting Information Available: Choice of the DNA model; validation of the DNA−gold model; XPS spectra for gold surfaces; simulated effect of model gold−DNA interaction parameters on DNA melting temperature; 1D PMF of hybridization in

bulk; normalized probability distributions of the end-to-end distance of the target strand on gold surface in C-state; 1D potential of mean forces. The Supporting Information is available free of charge on the ACS Publications website at DOI: 10.1021/acsnano.5b02530.

REFERENCES AND NOTES

1. Levicky, R.; Horgan, A. Physicochemical Perspectives on DNA Microarray and Biosensor Technologies. *Trends Biotechnol.* **2005**, *23*, 143–149.
2. Mir, K. U.; Southern, E. M. Sequence Variation in Genes and Genomic DNA: Methods for Large-Scale Analysis. *Annu. Rev. Genomics Hum. Genet.* **2000**, *1*, 329–360.
3. Homola, J. Surface Plasmon Resonance Sensors for Detection of Chemical and Biological Species. *Chem. Rev.* **2008**, *108*, 462–493.
4. Chan, V.; Graves, D. J.; McKenzie, S. E. The Biophysics of DNA Hybridization with Immobilized Oligonucleotide Probes. *Biophys. J.* **1995**, *69*, 2243–2255.
5. Peterson, A. W.; Heaton, R. J.; Georgiadis, R. M. The Effect of Surface Probe Density on DNA Hybridization. *Nucleic Acids Res.* **2001**, *29*, 5163–5168.
6. Peterson, A. W.; Wolf, L. K.; Georgiadis, R. M. Hybridization of Mismatched or Partially Matched DNA at Surfaces. *J. Am. Chem. Soc.* **2002**, *124*, 14601–14607.
7. Shchepinov, M. S.; Case-Green, S. C.; Southern, E. M. Steric Factors Influencing Hybridisation of Nucleic Acids to Oligonucleotide Arrays. *Nucleic Acids Res.* **1997**, *25*, 1155–1161.
8. Gong, P.; Levicky, R. DNA Surface Hybridization Regimes. *Proc. Natl. Acad. Sci. U.S.A.* **2008**, *105*, 5301–5306.
9. Steel, A.; Levicky, R.; Herne, T.; Tarlov, M. J. Immobilization of Nucleic Acids at Solid Surfaces: Effect of Oligonucleotide Length on Layer Assembly. *Biophys. J.* **2000**, *79*, 975–981.
10. Schreiner, S. M.; Shudy, D. F.; Hatch, A. L.; Opdahl, A.; Whitman, L. J.; Petrovykh, D. Y. Controlled and Efficient Hybridization Achieved with DNA Probes Immobilized Solely through Preferential DNA-Substrate Interactions. *Anal. Chem.* **2010**, *82*, 2803–2810.
11. Glazer, M. I.; Fidanza, J. A.; McGall, G. H.; Trulson, M. O.; Forman, J. E.; Frank, C. W. Kinetics of Oligonucleotide Hybridization to DNA Probe Arrays on High-Capacity Porous Silica Substrates. *Biophys. J.* **2007**, *93*, 1661–1676.
12. Chen, C.; Wang, W.; Ge, J.; Zhao, X. S. Kinetics and Thermodynamics of DNA Hybridization on Gold Nanoparticles. *Nucleic Acids Res.* **2009**, *37*, 3756–3765.
13. Gao, Y.; Wolf, L. K.; Georgiadis, R. M. Secondary Structure Effects on DNA Hybridization Kinetics: A Solution *versus* Surface Comparison. *Nucleic Acids Res.* **2006**, *34*, 3370–3377.
14. Petty, T. J.; Wagner, C. E.; Opdahl, A. Influence of Attachment Strategy on the Thermal Stability of Hybridized DNA on Gold Surfaces. *Langmuir* **2014**, *30*, 15277–15284.
15. Levicky, R.; Herne, T. M.; Tarlov, M. J.; Satija, S. K. Using Self-Assembly to Control the Structure of DNA Monolayers on Gold: A Neutron Reflectivity Study. *J. Am. Chem. Soc.* **1998**, *120*, 9787–9792.
16. Gong, P.; Lee, C.-Y.; Gamble, L. J.; Castner, D. G.; Grainger, D. W. Hybridization Behavior of Mixed DNA/Alkylthiol Monolayers on Gold: Characterization by Surface Plasmon Resonance and ^{32}P Radiometric Assay. *Anal. Chem.* **2006**, *78*, 3326–3334.
17. Špringer, T.; Šípová, H.; Vaisocherová, H.; Štěpánek, J.; Homola, J. Shielding Effect of Monovalent and Divalent Cations on Solid-Phase DNA Hybridization: Surface Plasmon Resonance Biosensor Study. *Nucleic Acids Res.* **2010**, *38*, 7343–7351.
18. Alligrant, T. M.; Nettleton, E. G.; Crooks, R. M. Electrochemical Detection of Individual DNA Hybridization Events. *Lab Chip* **2013**, *13*, 349–354.
19. Love, J. C.; Estroff, L. A.; Kriebel, J. K.; Nuzzo, R. G.; Whitesides, G. M. Self-Assembled Monolayers of Thiolates on Metals As a Form of Nanotechnology. *Chem. Rev.* **2005**, *105*, 1103–1170.
20. Li, H.; Rothberg, L. Colorimetric Detection of DNA Sequences Based on Electrostatic Interactions with Unmodified Gold Nanoparticles. *Proc. Natl. Acad. Sci. U.S.A.* **2004**, *101*, 14036–14039.
21. Kimura-Suda, H.; Petrovykh, D. Y.; Tarlov, M. J.; Whitman, L. J. Base-Dependent Competitive Adsorption of Single-Stranded DNA on Gold. *J. Am. Chem. Soc.* **2003**, *125*, 9014–9015.
22. Herne, T. M.; Tarlov, M. J. Characterization of DNA Probes Immobilized on Gold Surfaces. *J. Am. Chem. Soc.* **1997**, *119*, 8916–8920.
23. Steel, A. B.; Herne, T. M.; Tarlov, M. J. Electrochemical Quantitation of DNA Immobilized on Gold. *Anal. Chem.* **1998**, *70*, 4670–4677.
24. Ge, D.; Wang, X.; Williams, K.; Levicky, R. Thermostable DNA Immobilization and Temperature Effects on Surface Hybridization. *Langmuir* **2012**, *28*, 8446–8455.
25. Zhou, D.; Sinniah, K.; Abell, C.; Rayment, T. Use of Atomic Force Microscopy for Making Addresses in DNA Coatings. *Langmuir* **2002**, *18*, 8278–8281.
26. Zafar, S.; Khater, M.; Jain, V.; Ning, T. A Comparison between Bipolar Transistor and Nanowire Field Effect Transistor Biosensors. *Appl. Phys. Lett.* **2015**, *106*, 063701.
27. Stern, E.; Klemic, J. F.; Routenberg, D. A.; Wyrembak, P. N.; Turner-Evans, D. B.; Hamilton, A. D.; LaVan, D. A.; Fahmy, T. M.; Reed, M. A. Label-Free Immunodetection with CMOS-Compatible Semiconducting Nanowires. *Nature* **2007**, *445*, 519–522.
28. Zafar, S.; D'Emic, C.; Afzali, A.; Fletcher, B.; Zhu, Y.; Ning, T. Optimization of pH Sensing Using Silicon Nanowire Field Effect Transistors with HfO_2 as the Sensing Surface. *Nanotechnology* **2011**, *22*, 405501.
29. Dorvel, B. R.; Reddy, B., Jr.; Go, J.; Duarte Guevara, C.; Salm, E.; Alam, M. A.; Bashir, R. Silicon Nanowires with High-k Hafnium Oxide Dielectrics for Sensitive Detection of Small Nucleic Acid Oligomers. *ACS Nano* **2012**, *6*, 6150–6164.
30. Ebers, J.; Moll, J. L. Large-Signal Behavior of Junction Transistors. *Proc. IRE* **1954**, *42*, 1761–1772.
31. Petrovykh, D. Y.; Kimura-Suda, H.; Whitman, L. J.; Tarlov, M. J. Quantitative Analysis and Characterization of DNA Immobilized on Gold. *J. Am. Chem. Soc.* **2003**, *125*, 5219–5226.
32. Anne, A.; Demaille, C. Dynamics of Electron Transport by Elastic Bending of Short DNA Duplexes. Experimental Study and Quantitative Modeling of the Cyclic Voltammetric Behavior of 3′-Ferrocenyl DNA End-Grafted on Gold. *J. Am. Chem. Soc.* **2006**, *128*, 542–557.
33. Kelley, S. O.; Barton, J. K.; Jackson, N. M.; McPherson, L. D.; Potter, A. B.; Spain, E. M.; Allen, M. J.; Hill, M. G. Orienting DNA Helices on Gold Using Applied Electric Fields. *Langmuir* **1998**, *14*, 6781–6784.
34. Kaiser, W.; Rant, U. Conformations of End-Tethered DNA Molecules on Gold Surfaces: Influences of Applied Electric Potential, Electrolyte Screening, and Temperature. *J. Am. Chem. Soc.* **2010**, *132*, 7935–7945.
35. Monserud, J. H.; Schwartz, D. K. Mechanisms of Surface-Mediated DNA Hybridization. *ACS Nano* **2014**, *8*, 4488–4499.
36. Barhoumi, A.; Zhang, D.; Halas, N. J. Correlation of Molecular Orientation and Packing Density in a dsDNA Self-Assembled Monolayer Observable with Surface-Enhanced Raman Spectroscopy. *J. Am. Chem. Soc.* **2008**, *130*, 14040–14041.
37. Sicard, F.; Destainville, N.; Manghi, M. DNA Denaturation Bubbles: Free-Energy Landscape and Nucleation/Closure Rates. *J. Chem. Phys.* **2015**, *142*, 034903.
38. Palmeri, J.; Manghi, M.; Destainville, N. Thermal Denaturation of Fluctuating Finite DNA Chains: The Role of Bending Rigidity in Bubble Nucleation. *Phys. Rev. E* **2008**, *77*, 011913.
39. Spiriti, J.; Kamberaj, H.; de Graff, A. M. R.; Thorpe, M. F.; van der Vaart, A. DNA Bending through Large Angles Is Aided by Ionic Screening. *J. Chem. Theory Comput.* **2012**, *8*, 2145–2156.
40. Ravan, H.; Kashanian, S.; Sanadgol, N.; Badoei-Dalfard, A.; Karami, Z. Strategies for Optimizing DNA Hybridization on Surfaces. *Anal. Biochem.* **2014**, *444*, 41–46.

41. Duan, H.; Winston, D.; Yang, J. K. W.; Cord, B. M.; Manfrinato, V. R.; Berggren, K. K. Sub-10-nm Half-Pitch Electron-Beam Lithography by Using Poly(methyl methacrylate) as a Negative Resist. *J. Vac. Sci. Technol., B* **2010**, *28*, C6C58–C6C62.
42. Wu, W.; Tong, W. M.; Bartman, J.; Chen, Y.; Walmsley, R.; Yu, Z.; Xia, Q.; Park, I.; Picciotto, C.; Gao, J. Sub-10 nm Nanoimprint Lithography by Wafer Bowing. *Nano Lett.* **2008**, *8*, 3865–3869.
43. Park, S.-M.; Liang, X.; Harteneck, B. D.; Pick, T. E.; Hiroshiba, N.; Wu, Y.; Helms, B. A.; Olynick, D. L. Sub-10 nm Nanofabrication *via* Nanoimprint Directed Self-Assembly of Block Copolymers. *ACS Nano* **2011**, *5*, 8523–8531.
44. Fernández-Regúlez, M.; Evangelio, L.; Lorenzoni, M.; Fraxedas, J.; Pérez-Murano, F. Sub-10 nm Resistless Nanolithography for Directed Self-Assembly of Block Copolymers. *ACS Appl. Mater. Interfaces* **2014**, *6*, 21596–21602.
45. Hinckley, D. M.; Freeman, G. S.; Whitmer, J. K.; de Pablo, J. J. An Experimentally-Informed Coarse-Grained 3-Site-per-Nucleotide Model of DNA: Structure, Thermodynamics, and Dynamics of Hybridization. *J. Chem. Phys.* **2013**, *139*, No. 144903 .
46. Hinckley, D. M.; Lequieu, J. P.; de Pablo, J. J. Coarse-Grained Modeling of DNA Oligomer Hybridization: Length, Sequence, and Salt Effects. *J. Chem. Phys.* **2014**, *141*, 035102.
47. Lao, R.; Song, S.; Wu, H.; Wang, L.; Zhang, Z.; He, L.; Fan, C. Electrochemical Interrogation of DNA Monolayers on Gold Surfaces. *Anal. Chem.* **2005**, *77*, 6475–6480.
48. Plimpton, S. Fast Parallel Algorithms for Short-Range Molecular Dynamics. *J. Comput. Phys.* **1995**, *117*, 1–19.
49. Sugita, Y.; Okamoto, Y. Replica-Exchange Molecular Dynamics Method for Protein Folding. *Chem. Phys. Lett.* **1999**, *314*, 141–151.
50. Kumar, S.; Rosenberg, J. M.; Bouzida, D.; Swendsen, R. H.; Kollman, P. A. The Weighted Histogram Analysis Method for Free-Energy Calculations on Biomolecules. I. The Method. *J. Comput. Chem.* **1992**, *13*, 1011–1021.
51. Grossfield, A. WHAM: The weighted histogram analysis method, Version 2.0.9.